Apertif 1.4 GHz continuum observations of the Boötes field and their combined view with LOFAR

(article starts on next page)

Astronomy
&
Astrophysics

Apertif 1.4 GHz continuum observations of the Boötes field and their combined view with LOFAR[*]

A. M. Kutkin[1], T. A. Oosterloo[1,2], R. Morganti[1,2], A. R. Offringa[1,2], E. A. K. Adams[1,2], B. Adebahr[3], H. Dénes[4,1], K. M. Hess[1,5,6], J. M. van der Hulst[2], W. J. G. de Blok[1,7,2], A. Bozkurt[1], W. A. van Cappellen[1], A. W. Gunst[1], H. A. Holties[1], J. van Leeuwen[1], G. M. Loose[1], L. C. Oostrum[1,8,9], D. Vohl[1], S. J. Wijnholds[1], and J. Ziemke[1,10]

[1] ASTRON, The Netherlands Institute for Radio Astronomy, Oude Hoogeveensedijk 4, 7991 PD, Dwingeloo, The Netherlands
e-mail: kutkin@astron.nl
[2] Kapteyn Astronomical Institute, PO Box 800, 9700 AV Groningen, The Netherlands
[3] Astronomisches Institut der Ruhr-Universität Bochum (AIRUB), Universitätsstrasse 150, 44780 Bochum, Germany
[4] School of Physical Sciences and Nanotechnology, Yachay Tech University, Hacienda San José S/N, 100119 Urcuquí, Ecuador
[5] Instituto de Astrofísica de Andalucía (CSIC), Glorieta de la Astronomía s/n, 18008 Granada, Spain
[6] Department of Space, Earth and Environment, Chalmers University of Technology, Onsala Space Observatory, 43992 Onsala, Sweden
[7] Department of Astronomy, University of Cape Town, Private Bag X3, Rondebosch 7701, South Africa
[8] Anton Pannekoek Institute, University of Amsterdam, Postbus 94249, 1090 GE Amsterdam, The Netherlands
[9] Netherlands eScience Center, Science Park 140, 1098 XG Amsterdam, The Netherlands
[10] University of Oslo Center for Information Technology, PO Box 1059, 0316 Oslo, Norway

ABSTRACT

We present a new image of a 26.5 square degrees region in the Boötes constellation obtained at 1.4 GHz using the Aperture Tile in Focus (Apertif) system on the Westerbork Synthesis Radio Telescope. We use a newly developed processing pipeline that includes direction-dependent self-calibration, which provides a significant improvement in the quality of the images compared to those released as part of the Apertif first data release. For the Boötes region, we mosaicked 187 Apertif images and extracted a source catalog. The mosaic image has an angular resolution of $27 \times 11.5''$ and a median background noise of 40 µJy beam^{-1}. The catalog has 8994 sources and is complete down to the 0.3 mJy level. We combined the Apertif image with LOFAR images of the Boötes field at 54 and 150 MHz to study the spectral properties of the sources. We find a spectral flattening toward sources with a low flux density. Using the spectral index limits from Apertif nondetections, we derive that up to 9% of the sources have ultrasteep spectra with a slope below –1.2. A steepening of the spectral index with increasing redshift is also seen in the data, which shows a different dependence for the low- and high-frequency spectral index. The explanation probably is that a population of sources has concave radio spectra with a turnover frequency of about the LOFAR band. Additionally, we discuss cases of individual extended sources with an interesting resolved spectral structure. With the improved pipeline, we aim to continue to process data from the Apertif wide-area surveys and release the improved 1.4-GHz images of several well-known fields.

Key words. catalogs – surveys – radio continuum: general

1. Introduction

The APERture Tile In Focus (Apertif) is a phased-array feed (PAF) system for the Westerbork Synthesis Radio Telescope (WSRT) that was designed for performing wide-field surveys of the northern sky (van Cappellen et al. 2022). During its operations in 2019–2022, the Apertif surveys covered about 2300 square degrees (Hess et al., in prep.). The first imaging-data release took place in 2019 and is described in Adams et al. (2022).

One of the added values of the Apertif surveys is their synergy with the Low Frequency Array (LOFAR, van Haarlem et al. 2013) surveys. LOFAR provides radio images with a resolution of 6″ at 150 MHz (High Band Antenna, HBA; Shimwell et al. 2022) and with a resolution of 15″ at 50 MHz (Low Band

Antenna, LBA; de Gasperin et al. 2021, 2023). The resolution of the LBA is particularly close to that of the Apertif images. The comparable angular resolution and sensitivity (for spectral indices typical of extragalactic radio sources) of these three surveys combined provides information about the radio spectra of the sources at MHz to GHz frequencies. Some examples of results from these combinations are illustrated in Morganti et al. (2021a,b), Kutkin et al. (2022, hereafter K22), Shulevski et al. (in prep.), and Adebahr et al. (2022).

Well-known fields that are observed in multiple bands by a variety of telescopes are ideal regions for probing the spectral properties of radio sources because they also provide a wealth of ancillary data, most notably, host galaxy properties and redshifts. One such field for which the study of radio spectra can be expanded is the Boötes field (see the description of this field and the available ancillary data by Williams et al. 2021). Considering the availability of existing deep LOFAR HBA and LBA observations, this field is a prime target to be imaged at 1.4 GHz
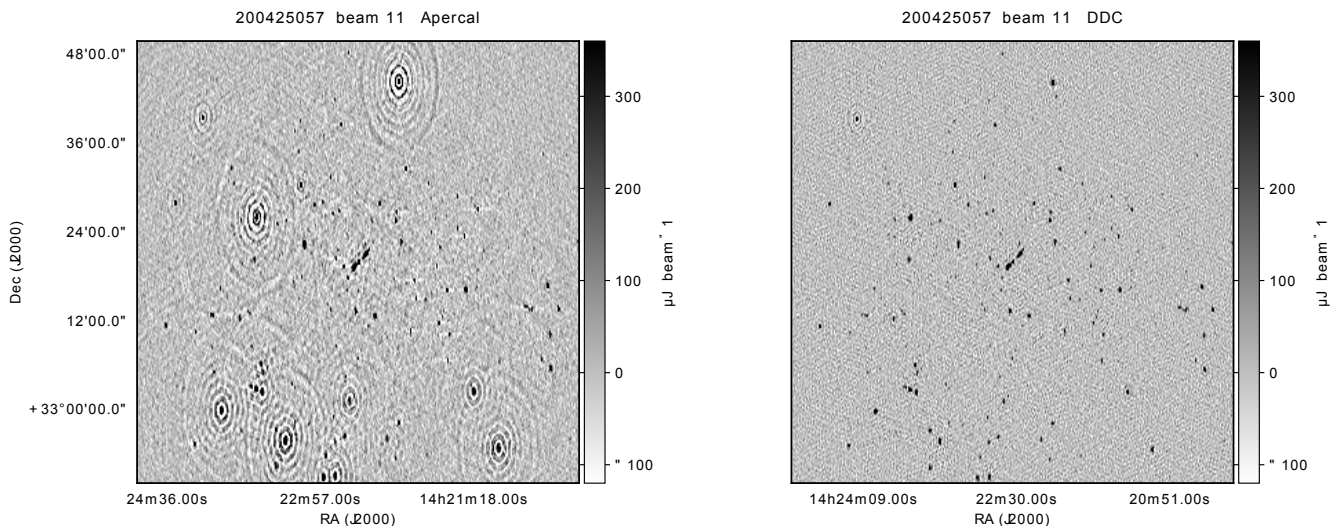
Fig. 1. Example of the improvement in image quality as the result of including direction-dependent effects in the calibration of Apertif data. Left panel: Apertif image obtained with the old direction-independent pipeline. Right panel: image made from the same data, but applying the new direction-dependent pipeline.

by Apertif in order to allow the analysis of the sources using three frequencies simultaneously.

Since the start of the study of radio sources, radio spectra have been recognized as a powerful tool for deriving important properties of their radio emission, such as the injection mechanism and the presence of absorption, and for tracing their history and evolution (Kardashev 1962; Scheuer & Williams 1968; Pacholczyk 1970; Carilli et al. 1991; Condon 1992; Morganti 2017). Although the spectral shape of radio sources can to first order be approximated by a power law ($S \propto \nu^{\alpha}$, where α is the spectral index), deviations from this simple form provide key signatures for tracing the physical and evolutionary properties of a radio source. For example, inverted spectral indices observed at low frequencies (i.e., a spectral index higher than that of the higher-frequency part of the spectrum) can indicate an absorption mechanism, such as free-free absorption, or synchrotron self-absorption, which might lead to a peaked shape of the spectrum. An important group of sources that can be identified in this way is that of young radio galaxies with newly born jets (see O'Dea & Saikia 2021, for a review). At the other extreme, for sources in which the central activity has stopped or decreased substantially (i.e., dying radio sources), the spectrum is expected to show a steeping that starts at higher frequencies, becoming ultrasteep (USS) with $\alpha \lesssim -1.2$ (Komissarov & Gubanov 1994; Slee et al. 2001). The identification of such objects helps to shed light on the evolution cycle of extragalactic radio sources. USS sources have also been used to pinpoint high-redshift radio galaxies through the observed trend between spectral index and redshift (see, e.g., Blumenthal & Miley 1979; Roettgering et al. 1994; Klamer et al. 2006; Morabito & Harwood 2018). In addition, spectral index images reveal different electron populations within a source (hotspots, remnant lobes, or tails) that provide clues about the ongoing process and the evolution of radio sources (e.g., Harwood et al. 2017).

Large and deep samples with observations covering multiple parts of the radio spectrum are an essential ingredient for identifying these extreme phases in the life of radio source so that a better inventory can be made of the relevance of the various processes. In this work, we present a new deep-continuum mosaic image and source catalog obtained at 1400 MHz with Apertif, covering the full area of the Boötes field that was imaged earlier

at 54 and 150 MHz by LOFAR (Williams et al. 2021; Tasse et al. 2021). Compared to the images of the First Apertif Data Release, the present study makes use of an improved processing pipeline that now includes direction-dependent calibration, which results in a much better image quality. Based on these new images, we analyze and discuss the spectral properties of the sources.

The description of the new pipeline is given in Sect. 2. The new image and the catalog are described in Sect. 3. The LOFAR data and further processing are described in Sect. 4. The spectral indices are analyzed and discussed in Sect. 5.

2. Processing pipeline

The default Apertif pipeline, `Apercal`[1], includes automatic calibration and imaging procedures (Adebahr et al. 2022). However, it provides only a direction-independent calibration, which in the case of Apertif, is often not sufficient for obtaining science-quality images. The resulting images often show direction-dependent effects (DDEs) arising from malfunctioning PAF elements. Faulty PAF elements effectively lead to large errors in the shape of a compound beam of a given antenna. In the case of the WSRT, these effects manifest themselves as concentric elliptical artifacts around the sources (see Fig. 1 for an example). These artifacts significantly reduce the dynamic range of the images and complicate the source-finding procedure. Overall, more than half of all Apertif images are affected by DDEs.

We have developed and applied a new procedure that includes both direction-independent (DI) and direction-dependent (DD) self-calibration to process Apertif data. It is based on the LOFAR default preprocessing pipeline (DPPP/DP3; van Diepen et al. 2018) and the `wsclean` imaging package (Offringa et al. 2014). The code and documentation of the new pipeline are available at GitLab[2].

The image of each compound beam of an observation is calibrated independently. The new pipeline starts with the pre-flagged cross-calibrated continuum visibilities produced with the initial steps of `Apercal`. For many of these data sets, additional flagging of antenna-beam combinations is made for which the DD errors are very large. Following this, a DI calibration is

---

[1] https://github.com/apertif/apercal
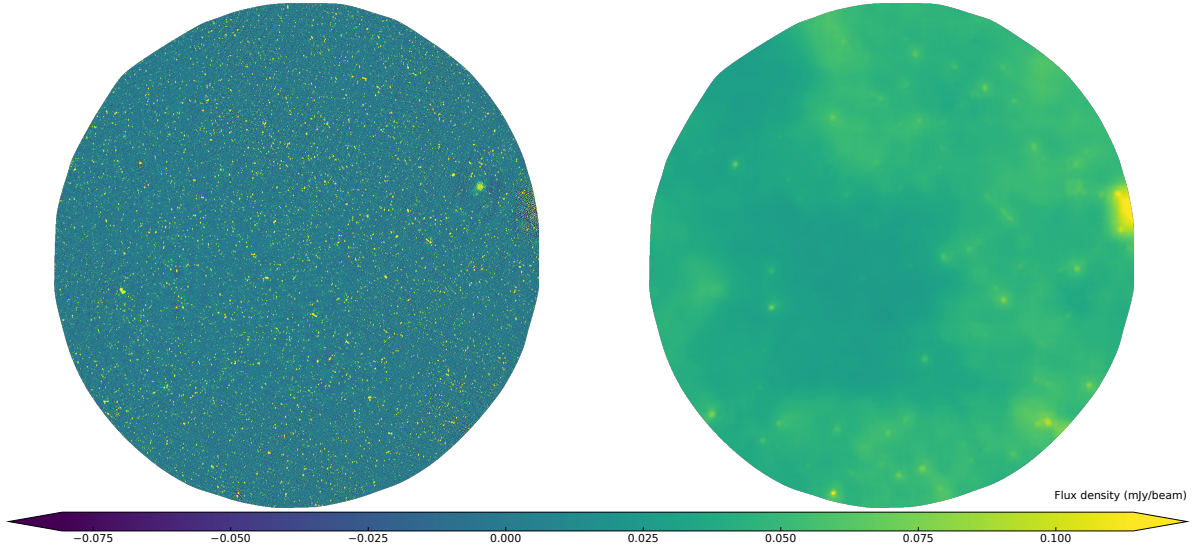[2] https://git.astron.nl/kutkin/apipeline

Fig. 2. Apertif mosaic of the Boötes region and the noise RMS map. The sky coverage matches that of the LOFAR HBA deep-field image. The image is centered at RA = $14^{\rm h}31^{\rm m}53^{\rm s}$, Dec = $+34°27'43''$ and covers an area of 26.5 square degrees.

performed. This step includes three cycles of self-calibration and imaging. First, a phase-only self-calibration with a 10-minute solution interval is run, followed by a phase-only calibration with a 30-s solution interval. The final step in the DI calibration is an amplitude and phase calibration with a long solution interval of one hour. The second and third `CLEAN` step in the DI self-calibration are done using masks based on the local signal-to-noise ratio estimated from the residual images of the previous step. The number of substeps, the type of the calibration, the parameters for creating the local noise images, and the solution intervals were determined before running the pipeline on all images by manually experimenting with these parameters and analyzing the results through the validation procedure described in Adams et al. (2022). This resulted in a final set of parameters that was used for all images.

After the DI calibration, a clustering procedure is performed. The final `CLEAN` model obtained after the DI calibration is segmented using Voronoi tessellation, for which the cluster centers located at the 10 brightest sources. With this segmented model, DD calibration is performed by calibrating each segment independently. This step is performed using DP3 `ddecal` with the parameter `subtract=True`, meaning that the visibilities are subtracted from the DI calibrated data with the DD calibration solutions applied. The residual visibilities, free from DDEs, are then imaged, and the final DI model is restored on this image. This final compound-beam image is produced with a size of 3072×3072 pixels and a pixel scale of $3''$.

To illustrate the quality improvement over images produced with the original DI pipeline, Fig. 1 shows an image obtained with this original DI pipeline as well as the image made from the same data, but using the new DD pipeline. The elliptical artifacts due to DDEs in the image that was produced with the original pipeline have been corrected for, and the quality of the images has significantly improved. The flux density of the sources does not differ by more than a few percent between the images.

3. Apertif image and catalog

3.1. Mosaic image

We focus on a sky area of approximately 30 square degrees of the Boötes field as observed with LOFAR (see Sect. 4).

This area has been covered by Apertif with 187 compound-beam images from eight different survey observations performed between April 2019 and November 2021. The self-calibration and imaging procedure was performed with the newly developed pipeline described in Sect. 2. The DD calibration allowed us to achieve a significant improvement of the quality of the individual images (as shown in Fig. 1). This is quantified by the fraction of compound-beam images that pass the Apertif quality validation (see Adams et al. 2022 for details), which increased from 40% using the default pipeline to 98% with the new pipeline.

To obtain the final mosaic image, the astrometric accuracy of the images was first improved by cross-matching sources from each individual image with those in the LOFAR HBA image (labeled M2 and described in Sect. 4) and by correcting the astrometry of the Apertif images with the median position offset. The typical offset was found to be about $1''$ with only a few exceptions. After this, the images were combined in the standard way using the `amosaic`[3] mosaic package described in K22. This procedure includes a correction of the images for the compound-beam shapes (we use the same beam models here as in K22) that reconvolves the images to a common angular resolution and reprojects them onto the common sky grid. Because individual Apertif images overlap, the mosaicking leads to an increase in sensitivity. The mosaic image is shown in the left panel of Fig. 2, and the noise map is shown in the right panel of this figure. The angular resolution of the mosaic image is $27'' \times 11''.5$. The local noise varies over the image between 25 μJy beam^{-1} and 50 μJy beam^{-1}, with a median value of 40 μJy beam^{-1}. The image is available for download at https://vo.astron.nl.

3.2. The catalog

We extracted the Apertif source catalog (C1) using the Python Blob Detector and Source Finder (PyBDSF; Mohan & Rafferty 2015). Similar to Shimwell et al. (2019), we used a peak and island detection threshold of 5 σ and 4 σ, respectively, and the size of a sliding box to estimate the local RMS was set to $30 \times 30 \times b_{\rm maj}$, where $b_{\rm maj}$ is the major axis of the synthesized beam. This size was set to automatically decrease to $12 \times 12 \times b_{\rm maj}$ near bright sources to capture noise

---

[3] https://github.com/akutkin/amosaic

Table 1. Apertif source catalog.

Name	RA	σ_{RA}	Dec	σ_{Dec}	S_{total}	$\sigma_{S_{total}}$	S_{peak}	$\sigma_{S_{peak}}$	Maj	σ_{Maj}	Min	σ_{Min}	PA	σ_{PA}	RMS	S_Code
	(°)	('')	(°)	('')	mJy	mJy	mJy bm^{-1}	mJy bm^{-1}	('')	('')	('')	('')	(°)	(°)	μJy bm^{-1}	(S/M/C)
(1)	(2)	(3)	(4)	(5)	(6)	(7)	(8)	(9)	(10)	(11)	(12)	(13)	(14)	(15)	(16)	(17)
APTF_J142347+360215	215.9489	1.7	36.0378	1.0	5.28	0.37	1.68	0.10	78.1	3.6	0.0	2.8	−18.3	1.5	51.2	M
APTF_J142347+334237	215.9491	1.7	33.7103	2.5	0.54	0.11	0.40	0.05	14.8	7.6	6.3	5.3	−1.8	16.6	49.0	S
APTF_J142348+333741	215.9505	1.7	33.6281	2.3	0.42	0.09	0.39	0.05	0.0	16.1	0.0	6.9	…	…	50.0	S
APTF_J142348+325706	215.9506	1.1	32.9519	1.1	1.67	0.13	1.53	0.09	0.0	7.8	0.0	5.4	…	…	53.3	S
APTF_J142348+360527	215.9512	1.4	36.0911	1.4	8.50	0.53	1.81	0.10	63.6	3.7	12.0	3.0	−53.1	3.7	51.0	M
APTF_J142348+345034	215.9513	1.0	34.8429	0.9	2.03	0.13	1.71	0.10	9.0	1.4	0.0	3.3	−57.9	13.1	43.6	S
APTF_J142348+331951	215.9513	1.5	33.3309	2.0	0.46	0.09	0.45	0.05	0.0	12.6	0.0	3.2	…	…	47.3	S
APTF_J142348+345502	215.9514	1.1	34.9174	1.0	1.46	0.11	1.33	0.08	6.7	3.2	3.5	1.4	10.6	12.6	43.9	S
APTF_J142348+324234	215.9519	1.8	32.7095	2.5	0.51	0.12	0.43	0.06	7.6	10.0	4.6	3.0	53.7	75.9	59.3	S
APTF_J142348+364920	215.9529	1.1	36.8223	1.1	2.25	0.16	1.60	0.09	19.0	2.2	4.4	1.3	11.2	3.9	52.2	S
APTF_J142348+323548	215.9529	1.1	32.5968	1.1	1.96	0.16	1.69	0.11	8.5	2.6	0.0	5.5	58.2	26.6	67.1	S
APTF_J142348+332547	215.9538	1.3	33.4297	1.5	0.91	0.11	0.80	0.06	8.2	5.0	1.2	5.2	41.8	37.8	51.3	S
APTF_J142348+321540	215.9540	1.1	32.2613	1.1	1.50	0.12	1.44	0.09	5.2	4.1	0.0	3.6	−27.3	29.1	56.2	S

Notes. Sample of the catalog records. The columns are described in Sect. 3. The full table containing 8994 entries is available in machine-readable format at `https://vo.astron.nl` and through the CDS.

variations more accurately. For consistency, the same PyBDSF settings were used for the smoothed images described below in Sect. 4. PyBDSF only provides fitting errors for the flux density and position measurements, and it gives incorrect values for the errors in deconvolved shape parameters. These errors were adjusted and recalculated in the same way as described in K22 (Appendix A).

An example of the catalog structure is shown in Table 1. The column designations are as follows: Cols. 1: Apertif source name; Cols. 2 and 4: RA and Dec; Cols. 3 and 5: RA and Dec errors; Cols. 6 and 8: total and peak flux density; Cols. 7 and 9: integrated and peak flux density uncertainties; and Cols. 10, 12, and 14: deconvolved major and minor source size and position angle. A source size value 0.0 means that the PSF cannot be deconvolved from the fitted source along the given axis, and the corresponding uncertainty represents an upper size-limit estimate. The position angle is given in degrees ranging from −90° to 90° west to east through north. When both major and minor sizes are given as 0.0, the position angle is omitted. Columns 11, 13, and 15: uncertainties of the major and minor source size and position angle; Col. 16: local background noise rms; and Col. 17: source type as classified by PyBDSF, with 'S' as an isolated source fitted with a single Gaussian; 'C' as sources that were fit by a single Gaussian, but are within an island of emission that also contains other sources, and 'M' as sources fit with multiple Gaussians. The resulting catalog contains 8994 sources, 8% of which were modeled with multiple Gaussians. This indicates a complex structure (`S_Code=M`). Almost all other sources were modeled with a single Gaussian (`S_Code=S`).

After compiling the catalog, we cross-matched it with the NRAO VLA Sky Survey (NVSS; Condon et al. 1998) to compare the flux density scale. The median total flux density ratio is 0.98. This provides an additional check on the calibration, mosaicking, and cataloging procedures.

3.3. Reliability and completeness

We estimated the reliability and completeness of the catalog in the same way as described in K22 (see their Sect. 5.5). The reliability was obtained from PyBDSF false detections in the inverted image within an assumption of a symmetric noise distribution. The number of false detections in the Apertif catalog does not exceed 1.5% over the full flux density range. The completeness was estimated by comparing the differential source counts
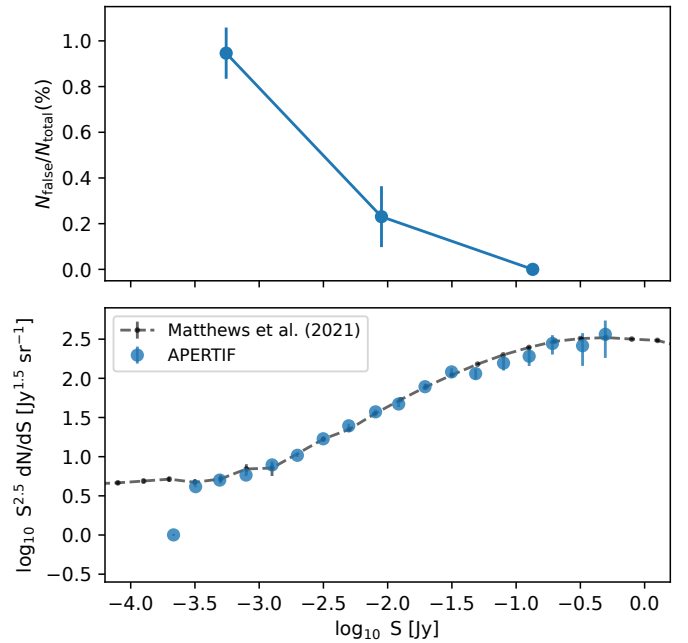

Fig. 3. False-detection fraction and differential source counts in the Apertif catalog.

corrected for the false-positive detection rate to the results published by Matthews et al. (2021), who provided comprehensive source counts over a wide flux density range at 1.4 GHz. The false-detection distribution and differential source counts as a function of total flux density are shown in Fig. 3. The catalog remains complete down to about 0.3 mJy. This level is calculated for the entire image, and a local completeness can be better because the local noise varies significantly over the mosaic (see Fig. 2).

4. LOFAR data and cross-matching of the catalogs

We used the publicly available LOFAR HBA and LBA mosaic images (referred to as M2 and M3 in the remainder of the paper and in Table 2) and the corresponding catalogs (C2 and C3) of the Boötes area (Tasse et al. 2021; Williams et al. 2021)[4].
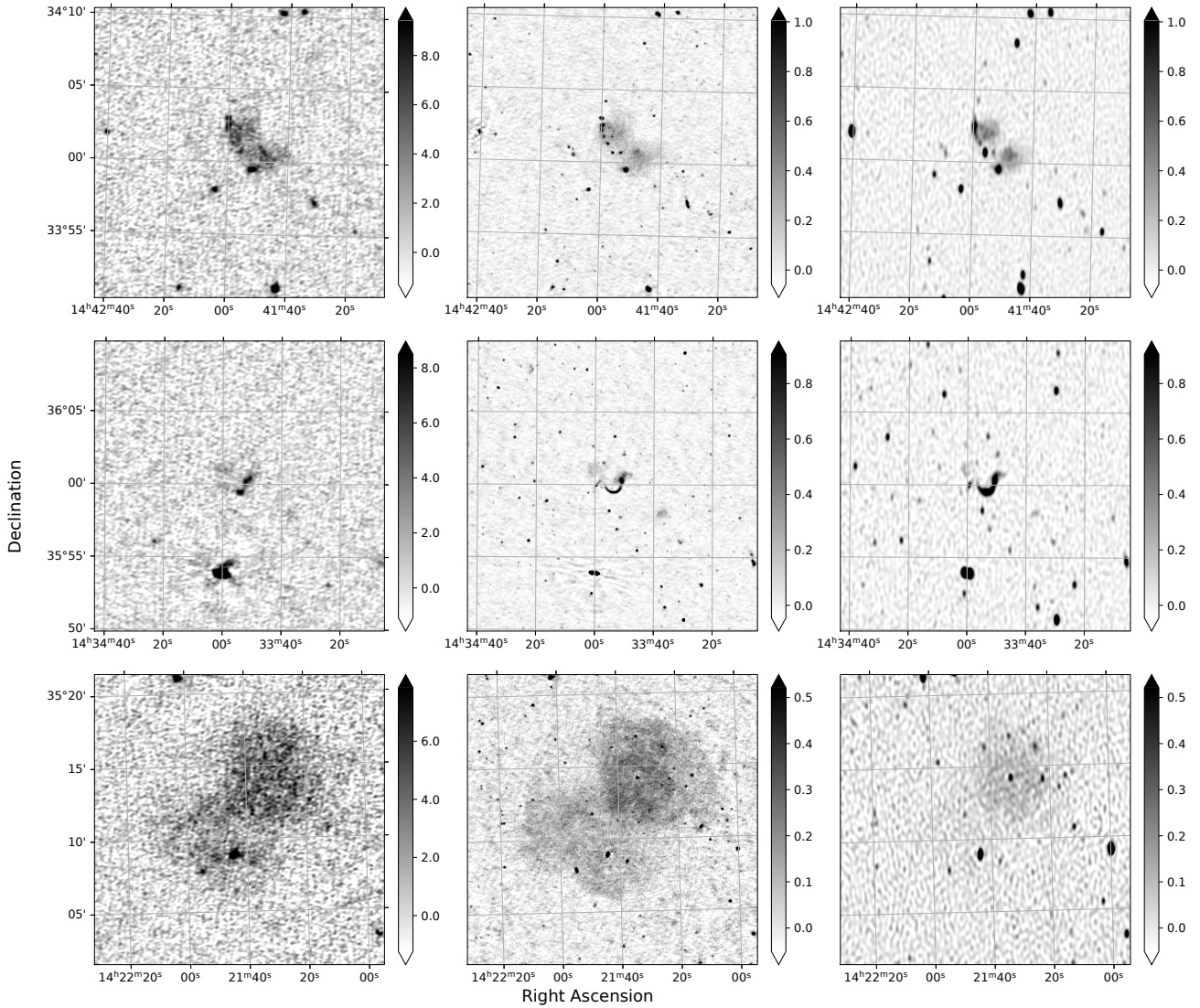
---

[4] `https://lofar-surveys.org/`

Fig. 4. Three images as seen by LBA (left column), HBA (middle column), and Apertif (right column). The color-bar scale is shown in mJy beam^{-1}.

Table 2. Images, catalogs, and their properties.

Instrument	Frequency (MHz)	Resolution ($''$)	N sources	Noise (μJy beam^{-1})	I/C
(1)	(2)	(3)	(4)	(5)	(6)
Apertif	1400	27×11.5	8994	40	M1/C1
LOFAR-HBA	150	6×6	36767	50	M2/C2
LOFAR-LBA	54	15×15	1948	1152	M3/C3
Apertif	1400	27×15	8742	42	M4/C4
LOFAR-HBA	150	27×15	8153	185	M5/C5
LOFAR-LBA	54	27×15	1675	1320	M6/C6

Notes. Columns designation: (1) instrument/survey; (2) approximate central frequency; (3) IMAGE resolution; (4) number of sources in the catalog; (5) median value of the noise RMS reported by PyBDSF; (6) mosaic image and catalog reference in the text.

Examples of sources as seen by LOFAR and Apertif are shown in Fig. 4. The object shown in the bottom row has been studied by de Gasperin et al. (2014). A new detailed study using the Apertif data as well will be presented by Adebahr et al. (2022).

A different angular resolution complicates a cross-matching of the catalogs, which leads to inaccurate spectral index measurements. This is especially significant when a source is resolved in one of the images and remains unresolved in another.

For the further analysis, we reprojected and smoothed the Apertif and LOFAR mosaic images to the same sky footprint and a common angular resolution of 27 × 15$''$.

The images and the corresponding catalogs (see below for a description) are listed in Table 2. In Col. 5 of this table, we report the median value of the background-noise RMS derived by PyBDSF at the locations of the sources (Isl_rms). A degrading resolution leads to an increase in the image noise, which has an especially strong impact on the HBA image M2. However, for the further analysis, the benefits of the images at the same resolution are more important.

We cross-matched catalogs C4, C5, and C6 using a 5$''$ matching radius. This resulted in 1286 sources that were in common between all three catalogs, 5605 sources in common between C4 and C5, and 1401 sources in common between C5 and C6.

5. Spectral indices

Taking advantage of the available images, we performed a detailed spectral index analysis. Hereafter, the spectral index between two surveys is defined as $\alpha_{\nu_2}^{\nu_1} = \ln(S_{\nu_1}/S_{\nu_2})/\ln(\nu_1/\nu_2)$,

Table 3. Spectral indices of the sources.

RA$_A$ (°) (1)	Dec$_A$ (°) (2)	$S_{A,int}$ (mJy) (3)	RA$_H$ (°) (4)	Dec$_H$ (°) (5)	$S_{H,int}$ (mJy) (6)	RA$_L$ (°) (7)	Dec$_L$ (°) (8)	$S_{L,int}$ (mJy) (9)	α_{high} (10)	$\sigma_{\alpha_{high}}$ (11)	α_{low} (12)	$\sigma_{\alpha_{low}}$ (13)	z (14)
215.7532	34.9463	0.3	...	...	...	...	...	...	>−0.63	...	...	...	...
215.9791	33.4191	0.4	215.9795	33.4185	2.0	...	...	...	-0.743	0.164	>−1.32	...	...
218.1798	32.3572	7.8	...	...	...	...	...	...	>0.83	...	>−1.07	...	...
218.2465	32.6096	0.3	218.2457	32.6089	2.2	...	...	...	−0.947	0.207	>−1.07	...	...
...	...	...	217.0903	34.4777	1.3	...	...	...	<−0.74	...	>−1.33	...	0.160
217.4835	35.3232	1.7	217.4825	35.3238	12.0	217.4830	35.3231	34.1	−0.882	0.051	−1.038	0.127	...
218.5853	32.8440	0.4	218.5850	32.8439	1.8	...	...	...	−0.708	0.151	>−1.17	...	...
218.7514	33.7390	14.0	218.7514	33.7389	95.7	218.7517	33.7392	240.6	−0.870	0.032	−0.917	0.073	...
...	...	...	215.3682	34.2739	14.6	...	...	...	<−1.68	...	>0.01	...	...
220.7384	35.2715	0.3	...	...	...	...	...	...	>−0.56	...	...	...	...

Notes. Extract of the cross-match table. Columns 1–9 represent RA, Dec and total flux density for C4, C5 and C6 catalogs respectively; Cols. 10–13 give spectral index and its error for Apertif-HBA and HBA-LBA frequencies respectively. When the total flux density measurement is missing in one of the catalogs, the spectral index limit is calculated using 5 times the local RMS as an upper limit on the source flux density at this frequency. Column 14 – redshift estimate of the corresponding HBA source. The full table containing 12756 entries is available in machine-readable format through CDS.

where S_{ν_1} and S_{ν_2} are the total flux density measurements, and ν_1, ν_2 are the corresponding survey frequencies (see Table 2). Having three frequencies, we also refer to α_{150}^{1400} and α_{54}^{150} as the high- and low-frequency spectral index, respectively, α_{high} and α_{low}.

In Table 3, we list the sources from the C4, C5, and C6 catalogs. When a source at a given location is present in the corresponding catalog, its coordinates and total flux density are given. When two flux density measurements are available, the spectral index is given along with its error. When a source is missing in one of the catalogs, a spectral index limit is estimated using five times the local RMS of the image with the missing source. In the last column, we give the redshift estimate, if available (see Sect. 5.3). We note that the three images are not contemporaneous, and some of the extreme apparent spectral indices can therefore reflect an intrinsic variability of the sources.

In Sects. 5.1–5.3, we discuss the spectral properties of the sources from Table 3. We also identify extended radio sources with interesting spectral index distributions and build their spectral index maps in Sect. 5.4.

5.1. The distribution at low and high frequencies

The distributions of the spectral indices α_{150}^{1400} and α_{54}^{150} for all sources are shown in Fig. 5, plotted as a function of the 150 MHz total flux density. The relatively better depth of the 150 MHz HBA survey means that weaker HBA sources can be detected in LBA and/or Apertif only when they have a suitable spectral index. We take these limits into consideration in the analysis presented in Sects. 5.2 and 5.4 and for the interpretation of the results. In Fig. 5, the dotted lines show the spectral index calculated for the C5 flux density and the completeness levels of C4 and C6 respectively (0.3 and 10 mJy), separating the regions where the distributions are incomplete due to the sensitivity limits of the Apertif and LBA surveys. Note that the completeness levels of the smoothed catalogs C4 and C6 are only slightly different from the ones of the original ones C1 and C3 (see noise values in Table 2).

The median values of α_{150}^{1400} and α_{54}^{150} calculated for the sources with HBA total flux density above 30 mJy, that is, not biased due to sensitivity limits, are $\alpha_{high} = −0.79 \pm 0.01$ and $\alpha_{low} = −0.80 \pm 0.02$, respectively (the errors here define a 90%

confidence interval calculated using bootstrapping). This is consistent with the results obtained in K22 (see the discussion and references therein for more details). The major scatter of the spectral index comes from intrinsic properties of the sources, while the median value remains robust. The distribution of the low-frequency spectral indices is similar to one obtained for the original catalogs C2 and C3 by Williams et al. (2021). These authors reported a trend of spectral flattening toward low flux density, which they explained by the increasing relative number of core-dominated compact AGN and star-forming galaxies (SFGs).

We binned the sources using their HBA total flux density into eight intervals (bins) and calculated the median spectral index in each bin. For every median value, we calculated the 90% confidence interval using a bootstrap approach. This was needed because the distribution of the spectral index inside a bin is non-Gaussian, especially at a lower flux density, where the completeness plays a role. The bin widths, median values of spectral index, and the corresponding 90% confidence intervals are shown in Fig. 5 with the error bars.

A trend of spectral flattening is indeed visible down to 10 mJy, in agreement within the errors with previous studies (e.g., Intema et al. 2011; Mahony et al. 2016; de Gasperin et al. 2018; Williams et al. 2021). The low-frequency spectral index α_{54}^{150} becomes significantly flatter than α_{150}^{1400} for sources with an HBA total flux density below 30 mJy (the leftmost bin in Fig. 5 is clearly affected by the incompleteness of LBA catalog C6). At the same time, the high-frequency spectral index remains below –0.75 for sources in all flux density bins. The spectral index over the full frequency span, α_{54}^{1400}, takes intermediate values between the two. The significant flattening of the median spectral index at lower frequencies can be explained by an increasing fraction of sources with concave radio spectra that peak around the lowest frequency (54 MHz). This scenario is also supported by analyzing the dependence of the spectral index on redshift (Sect. 5.3).

5.2. Color-color diagram

The availability of the data at three frequencies allows us to expand the analysis of the spectral index by building a color–color diagram of α_{150}^{1400} versus α_{54}^{150} calculated as described above.
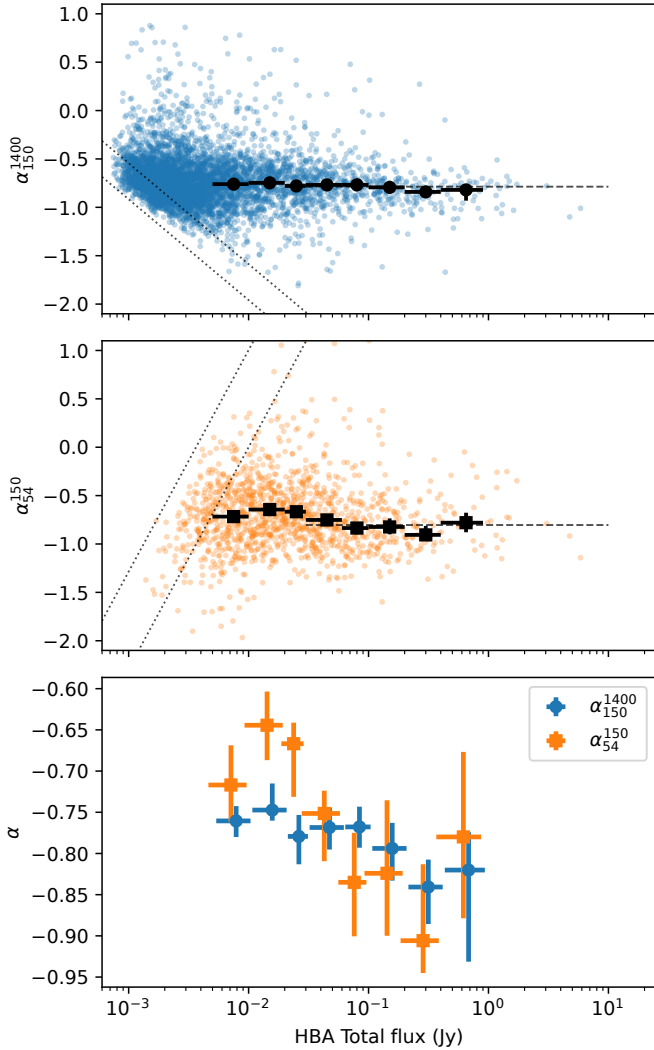
Fig. 5. Spectral indices measured between 1400 and 150 MHz (top) and 150 and 54 MHz (middle) vs. the 150 MHz HBA total flux density. The dotted lines define the spectral index limits calculated using the minimum total flux density and the completeness level of C4 and C6. The median values calculated for the sources above the completeness limits (−0.77 and −0.73) are shown with horizontal dashed lines. Markers with bars show the median spectral index calculated inside eight flux density bins (also shown separately in the bottom panel). The bins are shown with horizontal bars. The 90% confidence intervals of the median values derived using bootstrapping are shown with vertical bars.

The color–color diagram allowed us to identify groups of sources with extreme spectral indices or those that deviate from a single power law in the frequency range between the LBA and Apertif frequencies. This in turn provides information about the physical conditions of the sources.

The color–color plot is shown in Fig. 6. To minimize the number of artifacts and outliers that are due to a complex source structure, we required a source to have been fit by a single Gaussian (S_Code='S') and have $S/N > 15$ in HBA catalog C5. Although a large fraction of the sources is located on the 1:1 line, indicating that they are characterized by a power-law spectral distribution without major breaks, Fig. 6 shows that the spectral indices of a significant fraction of the sources deviates from this line, with the points being located below this line. This is particularly clear for the group of sources with a flatter spectrum ($-0.5 < \alpha_{54}^{150} < 1$) at low frequencies, which instead show

a steeper spectrum $-1 < \alpha_{150}^{1400} < 0.3$) at higher frequencies. A similar trend is also reported by Boehme et al. (in prep.), who cross-matched LOFAR data with other surveys.

To further investigate this trend, we expanded the color–color plot by deriving the limits to the spectral indices as well. When a source in C5 (HBA) had no counterpart in C4 (Apertif) or C6 (LBA), we estimated the limits of its spectral indices using the RMS noise of the corresponding images M4 and M6. The flux density limits were estimated using five times the noise at the location of the corresponding source in C5. These limits are shown in the right panel of Fig. 6. This addition to the original color–color diagram is useful for confirming the trend of sources with flatter spectral indices at low frequencies (Fig. 6, right) and complementing the distribution of the sources detected by all three surveys.

Thus, adding the limits has further confirmed that a group of sources shows a flattening at low frequency. Peaked spectrum sources, defined as having an inverted spectral index at low frequency ($\alpha_{low} > 0$) and a steep spectrum at high frequencies, are also found. A spectrum flattening or turnover at lower frequencies is also seen in Fig. 5 and might be a manifestation of absorption processes such as synchrotron self-absorption or free-free absorption. The corresponding sources can be both compact synchrotron sources and/or star-forming galaxies (Callingham et al. 2017; Galvin et al. 2018; O'Dea & Saikia 2021).

Another interesting group of sources in the color–color plot are the USS. Their spectral index is steeper than −1.2 at either low or high (or both) frequencies. The depth of the Apertif image, although not enough to directly detect many USS, allows us to place tight limits on the identification of a larger group of them. Because the Apertif flux limit is 200 μJy beam^{-1} (5σ noise of image M4) for a reliable source detection, the counterpart source with USS in image M5 should have a peak flux density $\gtrsim$2.8 mJy beam^{-1}. There are 2497 HBA sources with peak flux density above this limit. To avoid artifacts and sources with a complex structure, we further required them to be fit with a single Gaussian (S_Code="S") and have an $S/N > 15$ in catalog C4. This resulted in 1743 sources. With these restrictions, the fraction of USS sources including the limits from Apertif non-detections is about 6–9%.

A number of sources (110) have USS also at low frequencies, between 150 and 54 MHz. The nature of these sources is interesting because they can be particularly old remnant sources or high redshift sources. Thirty-eight of these sources have redshift estimates (see Sect. 5.3) with a maximum redshift of 5.22 and a median value of 1.37, suggesting that some of these USS sources could be at high z (but see Sect. 5.3). We note that a more careful redshift association might be needed to study individual sources.

At the same time, some of the USS sources at low frequencies are candidate remnants. This is illustrated by the fact that we find cases of sources with extended USS emission associated with low-redshift galaxies. For example, the diffuse source J142957+325516 has a low-frequency spectral index $\alpha_{low} = -1.8$ and an estimated redshift of $z = 0.24$. Other interesting examples of sources with extended USS emission are J143623+353430 at $z = 0.74$ and J143134+332321 at $z = 1.3$. These sources show properties that are characteristic of remnant radio sources, as discussed by Brienza et al. (2017) and Jurlin et al. (2021).

Other cases of extended objects in which only part of the emission is USS are discussed in Sect. 5.4 for sources larger than 1′. In these sources, the remnant emission appears to coexist with a new phase of activity, suggesting they are examples of restarted sources.
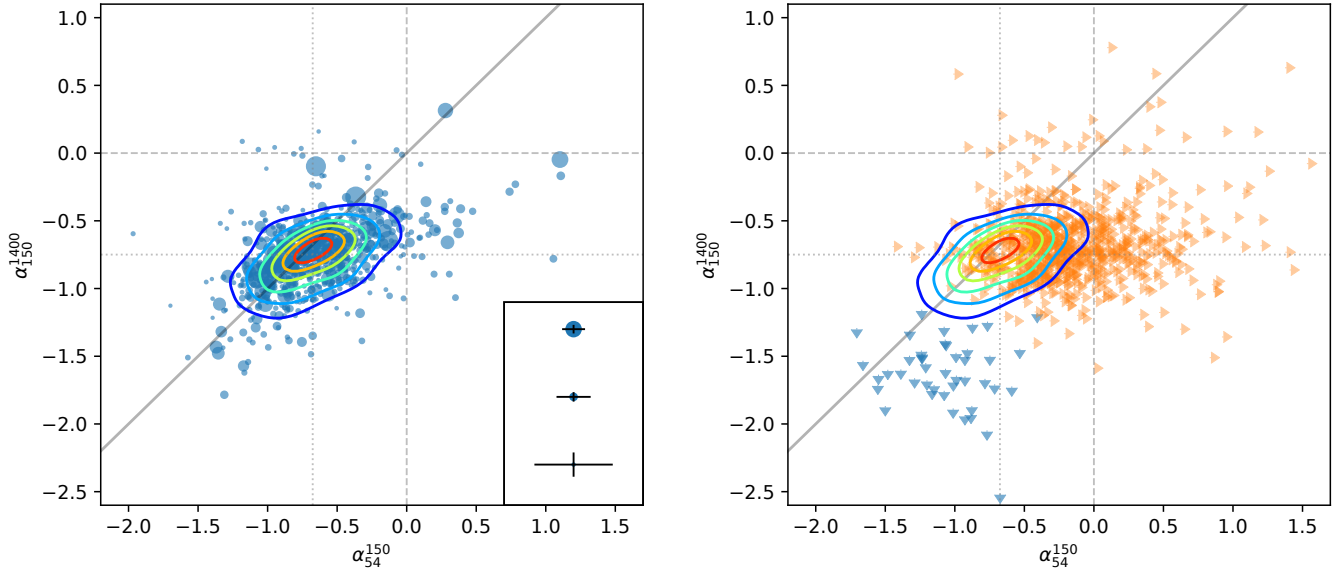
Fig. 6. Spectral index diagrams of all sources (see text for details). The left panel shows sources detected in catalogs C4, C5, and C6. The size of the markers is proportional to the source S/N in C5. The typical errors are shown in the bottom right corner. The right panel shows the spectral index limits of the sources that are missing in either C4 or C6 estimated from the noise RMS of images M4 and M6 at the location of a source. The contours show the Gaussian-kernel density estimate. The dashed lines indicates the zero spectral index, and the dotted lines show median values of α_{150}^{1400} and α_{54}^{150} calculated for the common sources.

We also found sources in the Apertif image that lack a counterpart in the LOFAR images. These sources have highly inverted spectra. An example is J144334.8+334012, which has an Apertif total flux density of 14 mJy, but has an upper limit of 0.35 mJy in the LOFAR HBA image, giving a lower limit of $\alpha_{150}^{1400} > 1.65$. This source was also detected in the Green Bank Telescope (GBT) survey at 4.85 GHz with a flux density of 34 mJy (Gregory & Condon 1991).

5.3. Spectral index and redshifts

As mentioned in the Introduction, a number of early studies have reported a correlation between spectral index and redshift and provided several possible explanations for this. However, there are also works in which no correlation was found (e.g., Calistro Rivera et al. 2017). It is interesting to probe this dependence using our data with redshift estimates available for a large number of sources.

We used the redshift estimate labels 'best' (zbest, spectroscopic or photometric) from the published value-added Boötes HBA catalog (Duncan et al. 2019; Kondapally et al. 2021). We cross-matched this catalog with C5 with a 5″ matching radius, resulting in more than 3000 redshift associations. These redshift estimates are given in the last column of Table 3. We note that due to the relatively low resolution of C5, there might be some cross-identification mistakes, and individual redshift estimates should be used with care.

The spectral index is plotted against redshift in Fig. 7 separately for Apertif-HBA, HBA-LBA, and Apertif-LBA frequency pairs. We estimated the probabilistic parameter distribution of a linear model fit to the data with a Markov chain Monte Carlo (MCMC) approach using the emcee package[5] (Foreman-Mackey et al. 2013). The model predictions for random samples from a posterior parameter distribution are drawn along with the maximum a posteriori (MAP) estimate. The corresponding linear

[5] https://emcee.readthedocs.io

Table 4. Parameters of the linear model fit $\alpha(z) = az + b$.

α	a	b
α_{150}^{1400}	$-0.024^{+0.003}_{-0.003}$	$-0.655^{+0.005}_{-0.004}$
α_{54}^{150}	$-0.023^{+0.012}_{-0.009}$	$-0.746^{+0.014}_{-0.018}$
α_{54}^{1400}	$-0.032^{+0.003}_{-0.004}$	$-0.719^{+0.006}_{-0.005}$
α_{150}^{1400}	$-0.028^{+0.013}_{-0.013}$	$-0.652^{+0.008}_{-0.008}$
α_{54}^{150}	$-0.187^{+0.052}_{-0.052}$	$-0.650^{+0.031}_{-0.030}$
α_{54}^{1400}	$-0.116^{+0.018}_{-0.015}$	$-0.675^{+0.009}_{-0.011}$

Notes. The first three rows correspond to the full redshift range, and the last three rows show the fit parameters for objects with $z < 1$. The errors indicate the 95% confidence interval for each parameter.

model coefficient is shown in the upper right corner of each panel with its 95% confidence interval.

The trend of spectral steepening with redshift is seen in all three data sets. The redshift dependence is different for the low- and high-frequency spectral index. The first drops steeply at lower redshifts and decreases more slowly at higher redshifts, and the second only shows a weak linear trend with a slope of ~0.03 throughout the entire redshift range. To illustrate this and to compare it with previous studies, we excluded objects with redshift higher than 1 from the sample and repeated the analysis. The obtained model parameters are listed in Table 4. The slope coefficients found for the last two models are similar to those reported by Morabito & Harwood (2018) for this redshift range ($0 < z < 1$).

A steeper redshift dependence for the low-frequency spectral index can be naturally explained if most sources have a peaked spectrum and the intrinsic spectral turnover frequency is close to the LBA one (54 MHz). In this case, the LBA flux density of a source is measured near the spectrum peak, and the resulting spectral index between the LBA and another frequency strongly
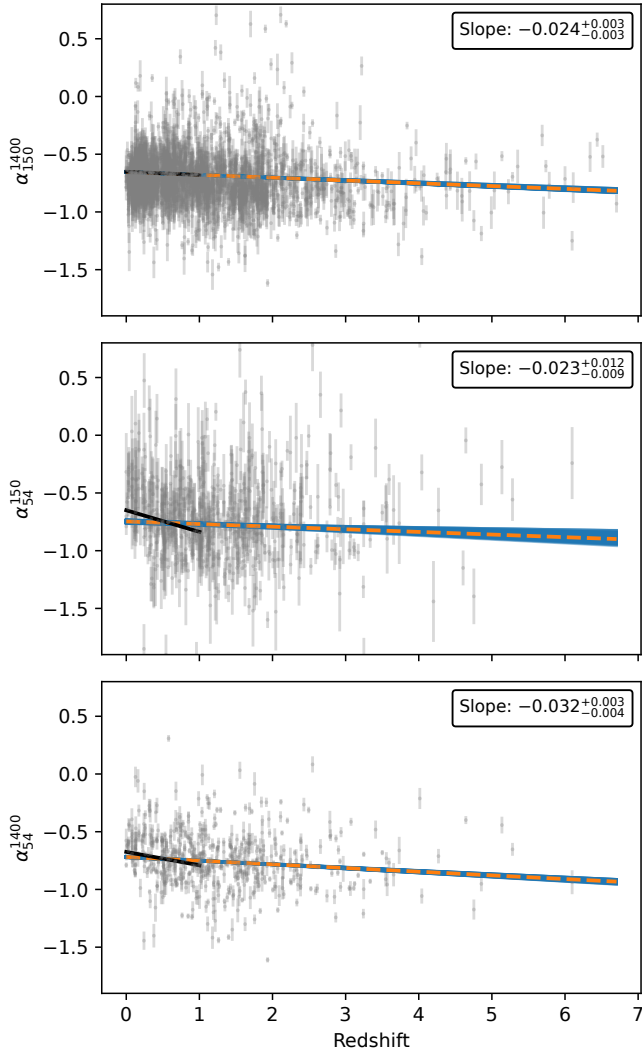
Fig. 7. Spectral index as a function of redshift. The solid lines show random samples drawn from an MCMC posterior distribution, and the dashed lines show the linear model with the MAP estimate. The corresponding slope coefficient is shown with its 95% confidence interval in the upper right corner. The same linear fit for $z < 1$ is shown with solid black lines. The parameters are given in Table 4.

depends on redshift. At the same time, the high-frequency spectral index does not trace the spectral turnover in most cases, and its redshift dependence remains weak. The overall common trend with a slope of ∼0.03 seen in all three samples can be attributed to spectral steepening due to more intense inverse Compton losses at higher redshifts or to a simple spectral index – luminosity correlation (see Morabito & Harwood 2018, for references).

We note that the sample considered here represents a complex mixture of sources with different types of spectra. For example, the Apertif-HBA cross-match sample contains more sources with flat or inverted spectra than the HBA-LBA sample, resulting in a different spectral index behavior between these groups. The increasing number of star-forming galaxies appearing at low redshifts might also play a role in the observed spectral flattening. Finally, the paucity of LBA-based spectral indices lower than –0.8 seen at low redshifts in Fig. 7 might be due to some systematic flux-scale offset for the LBA, but this is to be investigated outside of this work. To better understand the nature of the spectral index-redshift correlation, a separate

detailed study is required that takes the properties of various source populations into consideration.

5.4. Spectral index structure of selected extended sources

The analysis presented above is based on the integrated flux density of the sources detected by PyBDSF. However, through the good angular resolution of the available images, many extended sources can be seen, and the resolved spectral index images can be derived for them. Thus, one of the new exciting possibilities provided by joint Apertif and LOFAR surveys is to explore the structure of the spectral index within a source and connect this to the evolution of the radio source. The availability of three frequencies makes this analysis more challenging, but also more rewarding, allowing us to expand what was presented for the Lockman Hole (Morganti et al. 2021a,b).

To do this, we selected sources with a deconvolved size larger than 1′. This limit was chosen to be a few restoring beam sizes large to ensure that the spectral index structures are well resolved. In total, 74 sources larger than 1′ were found. The resulting sample is not large enough for a statistical study, but it allows us to investigate the spectral index structure in detail at least for some sources. For the purpose of this paper, we carried out most of the analysis and characterization of these resolved spectral indices by visual inspection.

Using images M4, M5, and M6, we constructed two spectral index maps of α_{150}^{1400} and α_{54}^{150}, respectively. Spectral index detections were derived for pixels with a signal at both frequencies above 3σ of the local noise. Instead, if at one frequency (typically LBA or Apertif) no detection was available, the limit was estimated by replacing the value of the pixels with the value of 3σ of the local noise. When both images were below 3σ, then the pixels were replaced with NaN values.

The 74 selected sources show a large variety of spectral index structures. In Figs. 8 and 9, we illustrate some of the more interesting cases. In these figures, we present (from left to right) the intensity LBA, HBA, and Apertif images, while the last two images show the spectral index distribution. The LBA total flux density contours are overlaid on the LBA-HBA spectral indices: Outside of these contours, the spectral index represents a lower limit. Empty contours and white color indicate regions in which both the LBA and HBA emission is below 3σ. The rightmost images show the high-frequency spectral index HBA-Apertif, and hte contours of the Apertif flux density are superposed. The spectral indices outside the contours (i.e., regions without an Apertif detection) should be considered as upper limits.

In Fig. 8, we show examples of the spectral index structure in FR I and FR II sources. The distribution follows what is expected for these sources, and it shows how the spectral index can help to classify the sources even when the total intensity shows a complex structure. The first two sources are FR I, and the spectral indices also indicate a relatively smooth distribution along the jets or lobes, as expected for this type of sources. The morphology of the third source is more difficult to classify because it has elements of both FR I and II. The spectral index indicates a possible hotspot in the southwest lobe that is more clearly seen at low frequencies, while no clear hotspot is seen in the northeast lobe.

Sources 4 and 5 in Fig. 8 are clear cases of FR II sources, with flat-spectrum emission at the edges of the lobes (where the hotspots are located) and steep spectrum emission in between, tracing the backflow emission deposited as the jet proceeds (i.e., resulting in the typical trend of older plasma situated closer to the core). Interestingly, the fifth source shows that this steep
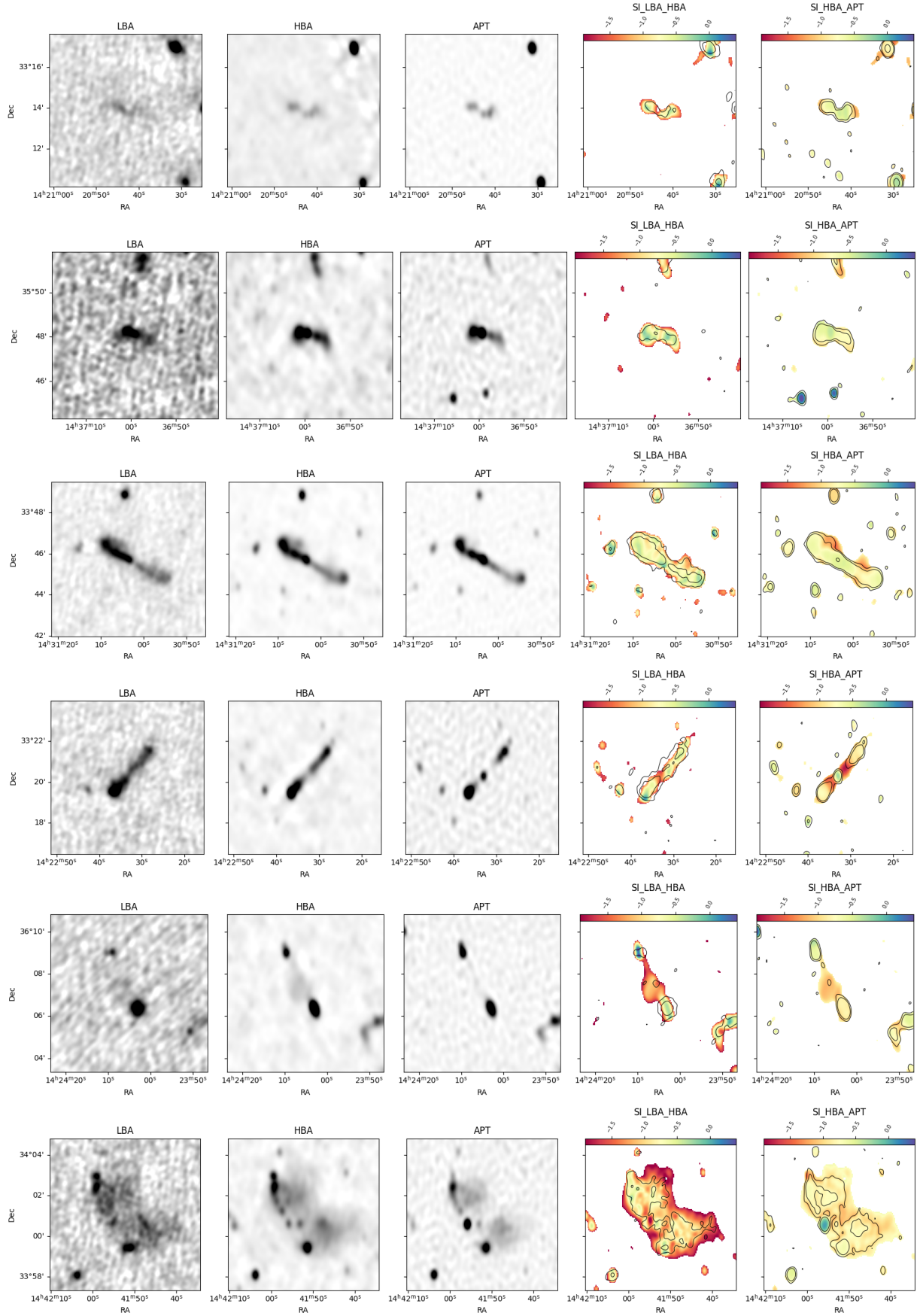
Fig. 8. Examples of FRI (top two) and FRII (third and fourth) radio sources where the extended spectral index can be studied. See the text for details. From left to right, we plot the LBA, HBA, and Apertif images, the spectral indices LBA-HBA (the LBS contours are superposed), and HBA-Apertif (the Apertif contours are superposed). The contour levels are 3, 10, and 150 σ, where σ is the local noise level of LBA (left) and Apertif image (right; see text).
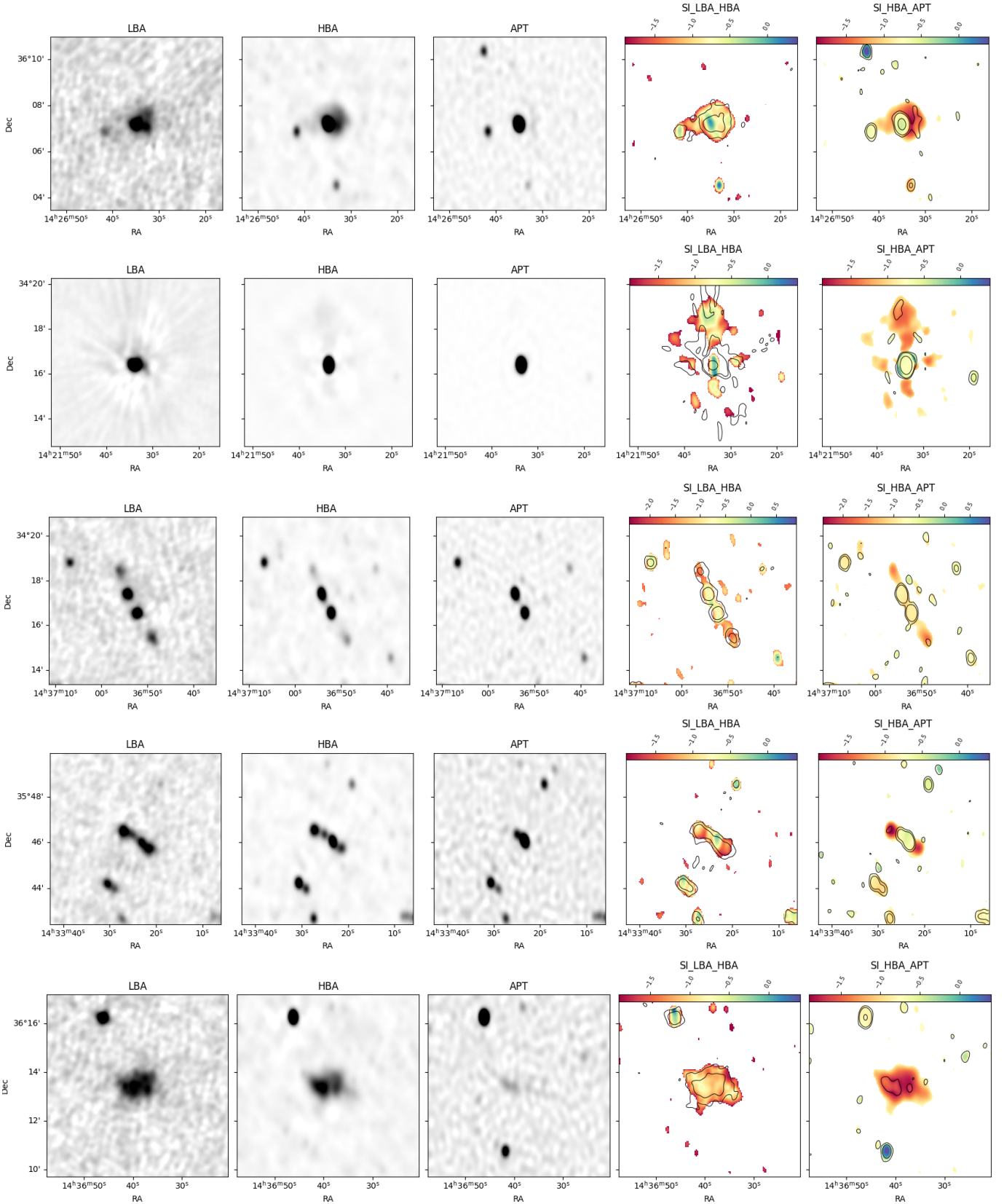
Fig. 9. Examples of sources with USS regions. The images and contours are the same as in Fig. 8. The top two show an active inverted spectrum core and a USS extended region. The third and fourth are double-double-type sources, where the outer is USS. All these sources can be considered as restarted. The last source is an example of a remnant source, in which the entire emission is USS.

spectrum emission (albeit not extreme; we note that the spectral indices at low frequencies are lower limits) extends perpendicular to the jet axis, perhaps indicating a change in its position angle in the past of the source or an interaction with a companion, as suggested, for example, for 3C 321, a well-studied radio galaxy with a similar radio morphology (Evans et al. 2008). The last source at the bottom of Fig. 8 is another complex case, suggesting an FR II structure, but with flat-spectrum hotspots at the end of the jets seen only at low frequencies, as well as a prominent core at high frequencies (which could also be a compact foreground source). The diffuse structure has a steep but not extreme spectral index and is suggestive of plasma tracing the motion of the source in a dense medium (perhaps a cluster or group).

Thus, the combination of morphology and spectral index adds more details to the classification based on the morphology alone, which makes the separation into FR I and II less sharp and more complex. Adding the information on the spectral index to the recent work by Mingo et al. (2019), who probed this dichotomy using LOFAR observations, may further explain the parameters influencing the radio morphology.

In addition to these sources, we also found a number of cases in which a large fraction (or even all) of the emission is USS, especially at high frequencies. As already discussed at the beginning of Sect. 5, these spectral properties are considered signatures of remnant emission of a previous phase of activity that has now stopped. In a number of cases, an active region coexists with the remnant region. This confirms what was found in the study of the Lockman Hole using LOFAR HBA and Apertif images and suggests that a dying phase has been followed by restarted activity. These radio sources are particularly interesting for our understanding of the evolution of radio galaxies.

In Fig. 9, we show some examples of these cases. The top two sources have active cores (which can be identified by flat or inverted spectra), while the extended emission around them is USS at high frequencies (most of the HBA-Apertif spectral index is an upper limit). Thus, the new phase of activity indicated by an active core appears to have started before the remnant emission has had time to disappear.

Sources 3 and 4 in Fig. 9, and in particular source 3, are examples of a double-double-like structure, in other words, sources with two sets of symmetric lobes likely resulting from two phases of activity (see, e.g., Mahatma et al. 2019, and references therein), at least as they appear in the HBA image. Interestingly, the outer pair of lobes is not seen in the Apertif image. These lobes were therefore characterized by an USS at high frequency (HBA-Apertif).

According to the calculations presented in Morganti et al. (2021b), USS at high frequencies (HBA-Apertif) imply ages of the remnants (i.e., the time passed since the last reacceleration of the electrons in a magnetic field of about $B_{eq} = 3\,\mu G$) to be in the range between 160 and 320 Myr. Within this period, a new phase of activity can start in these sources, as observed in the Lockman Hole (Morganti et al. 2021b).

The last source in Fig. 9 has an amorphous structure, and the entire emission is USS at high frequencies. We consider this a nice example of a remnant radio source. We do not find any extended source larger than $1'$ in which all emission is USS down to the lowest frequency. This may indicate that the remnant emission disappears below our detection limit for dying sources that are too old.

6. Conclusions

We have presented an image of a 26.5 square degrees region in the Boötes constellation obtained at 1.4 GHz using the Apertif system on the WSRT. This image was made using an improved calibration and imaging pipeline for Apertif. The main improvement offered by this new pipeline is that it incorporates direction-dependent calibration, allowing us to correct the Apertif images for imaging artifacts due to faulty PAF elements and to produce images of much higher quality compared to those of the first Apertif data release. With this pipeline, we processed 187 Apertif data sets and released a mosaic image matching the Boötes deep field observed earlier by the LOFAR telescope at 150 and 54 MHz. From the Apertif image, we compiled a source catalog containing 8994 sources, which is complete down to 0.3 mJy level.

We smoothed the Apertif image and the publicly available LOFAR images to the same angular resolution and created the matching catalogs to study spectral indices of the sources. The distribution of the low- and high-frequency spectral indices of the common sources, combined with limits, shows that most sources demonstrate a break or curvature in their spectra at low frequency.

We also investigated the dependence of the spectral indices on redshift and found a negative correlation, which can be explained as a K-correction of the spectra with a break or curvature at low frequencies. Using the color-color diagrams, we identified and discussed various types of interesting sources, including remnants, young AGN, and sources with restarted activity.

As shown in this work, the Apertif sensitivity and angular resolution provide a unique synergy with the LOFAR surveys at lower frequencies. The joint data analysis has a great potential for many astrophysical studies. The Apertif data continue to be processed, and we will focus on other LOFAR deep fields, such as the Elais-N1 and Lockman Hole area, for our future continuum releases.

References

Adams, E. A. K., Adebahr, B., de Blok, W. J. G., et al. 2022, A&A, 667, A38
Adebahr, B., Schulz, R., Dijkema, T. J., et al. 2022, Astron. Comput., 38, 100514
Astropy Collaboration (Robitaille, T. P., et al.) 2013, A&A, 558, A33
Astropy Collaboration (Price-Whelan, A. M., et al.) 2018, AJ, 156, 123
Blumenthal, G., & Miley, G. 1979, A&A, 80, 13
Boch, T., & Fernique, P. 2014, ASP Conf. Ser., 485, 277
Bonnarel, F., Fernique, P., Bienaymé, O., et al. 2000, A&AS, 143, 33
Brienza, M., Godfrey, L., Morganti, R., et al. 2017, A&A, 606, A98
Calistro Rivera, G., Williams, W. L., Hardcastle, M. J., et al. 2017, MNRAS, 469, 3468
Callingham, J. R., Ekers, R. D., Gaensler, B. M., et al. 2017, ApJ, 836, 174
Carilli, C. L., Perley, R. A., Dreher, J. W., & Leahy, J. P. 1991, ApJ, 383, 554
Condon, J. J. 1992, ARA&A, 30, 575
Condon, J. J., Cotton, W. D., Greisen, E. W., et al. 1998, AJ, 115, 1693
de Gasperin, F., Intema, H. T., Williams, W., et al. 2014, MNRAS, 440, 1542
de Gasperin, F., Intema, H. T., & Frail, D. A. 2018, MNRAS, 474, 5008
de Gasperin, F., Williams, W. L., Best, P., et al. 2021, A&A, 648, A104
de Gasperin, F., Edler, H. W., Williams, W. L., et al. 2023, A&A, 673, A165
Duncan, K. J., Sabater, J., Röttgering, H. J. A., et al. 2019, A&A, 622, A3
Evans, D. A., Fong, W.-F., Hardcastle, M. J., et al. 2008, ApJ, 675, 1057
Foreman-Mackey, D., Hogg, D. W., Lang, D., & Goodman, J. 2013, PASP, 125, 306
Galvin, T. J., Seymour, N., Marvil, J., et al. 2018, MNRAS, 474, 779
Gregory, P. C., & Condon, J. J. 1991, ApJS, 75, 1011
Harris, C. R., Millman, K. J., van der Walt, S. J., et al. 2020, Nature, 585, 357
Harwood, J. J., Hardcastle, M. J., Morganti, R., et al. 2017, MNRAS, 469, 639
Hunter, J. D. 2007, Comput. Sci. Eng., 9, 90
Intema, H. T., van Weeren, R. J., Röttgering, H. J. A., & Lal, D. V. 2011, A&A, 535, A38
Jurlin, N., Brienza, M., Morganti, R., et al. 2021, A&A, 653, A110
Kardashev, N. S. 1962, Soviet Ast., 6, 317
Klamer, I. J., Ekers, R. D., Bryant, J. J., et al. 2006, MNRAS, 371, 852
Komissarov, S. S., & Gubanov, A. G. 1994, A&A, 285, 27
Kondapally, R., Best, P. N., Hardcastle, M. J., et al. 2021, A&A, 648, A3
Kutkin, A. M., Oosterloo, T. A., Morganti, R., et al. 2022, A&A, 667, A39
Mahatma, V. H., Hardcastle, M. J., Williams, W. L., et al. 2019, A&A, 622, A13
Mahony, E. K., Morganti, R., Prandoni, I., et al. 2016, MNRAS, 463, 2997
Matthews, A. M., Condon, J. J., Cotton, W. D., & Mauch, T. 2021, ApJ, 909, 193
Mingo, B., Croston, J. H., Hardcastle, M. J., et al. 2019, MNRAS, 488, 2701
Mohan, N., & Rafferty, D. 2015, PyBDSF: Python Blob Detection and Source Finder, Astrophysics Source Code Library, [record ascl:1502.007]
Morabito, L. K., & Harwood, J. J. 2018, MNRAS, 480, 2726
Morganti, R. 2017, Nat. Astron., 1, 596
Morganti, R., Jurlin, N., Oosterloo, T., et al. 2021a, Galaxies, 9, 88
Morganti, R., Oosterloo, T. A., Brienza, M., et al. 2021b, A&A, 648, A9
O'Dea, C. P., & Saikia, D. J. 2021, A&ARv, 29, 3
Offringa, A. R., McKinley, B., Hurley-Walker, N., et al. 2014, MNRAS, 444, 606
Pacholczyk, A. G. 1970, Radio astrophysics. Nonthermal processes in galactic and extragalactic sources (San Francisco: Freeman)
Pandas development team 2020, https://doi.org/10.5281/zenodo.3509134
Pedregosa, F., Varoquaux, G., Gramfort, A., et al. 2011, J. Mach. Learn. Res., 12, 2825
Roettgering, H. J. A., Lacy, M., Miley, G. K., Chambers, K. C., & Saunders, R. 1994, A&AS, 108, 79
Scheuer, P. A. G., & Williams, P. J. S. 1968, ARA&A, 6, 321
Shimwell, T. W., Tasse, C., Hardcastle, M. J., et al. 2019, A&A, 622, A1
Shimwell, T. W., Hardcastle, M. J., Tasse, C., et al. 2022, A&A, 659, A1
Slee, O. B., Roy, A. L., Murgia, M., Andernach, H., & Ehle, M. 2001, AJ, 122, 1172
Tasse, C., Shimwell, T., Hardcastle, M. J., et al. 2021, A&A, 648, A1
van Cappellen, W. A., Oosterloo, T. A., Verheijen, M. A. W., et al. 2022, A&A, 658, A146
van Diepen, G., Dijkema, T. J., & Offringa, A. 2018, DPPP: Default Pre-Processing Pipeline, Astrophysics Source Code Library, [record ascl:1804.003]
van Haarlem, M. P., Wise, M. W., Gunst, A. W., et al. 2013, A&A, 556, A2
Virtanen, P., Gommers, R., Oliphant, T. E., et al. 2020, Nat. Methods, 17, 261
Williams, W. L., de Gasperin, F., Hardcastle, M. J. H., et al. 2021, A&A, 655, A40